Molten chloride salt technology for next-generation CSP plants: Compatibility of Fe-based alloys with purified molten MgCl$_2$-KCl-NaCl salt at 700 °C [1]

Qing Gong[1,*], Hao Shi[2], Yan Chai[1], Rui Yu[2,3], Alfons Weisenburger[2], Dihua Wang[3], Alexander Bonk[1], Thomas Bauer[4], Wenjin Ding[1]

[1]Institute of Engineering Thermodynamics, German Aerospace Center (DLR), Stuttgart, Germany
[2]Institute for Pulsed Power and Microwave Technology, Karlsruhe Institute of Technology (KIT), Eggenstein-Leopoldshafen, Germany
[3]School of Resources and Environmental Science, Wuhan University (WHU), Wuhan, PR China
[4]Institute of Engineering Thermodynamics, German Aerospace Center (DLR), Cologne, Germany
*Corresponding author:
Q. Gong (Tel.: +49 711 6862-8417, Email: qing.gong@dlr.de).

ABSTRACT

Molten chlorides, such as MgCl$_2$-KCl-NaCl, are promising advanced high-temperature (up to 800 °C) thermal energy storage (TES) materials in next-generation concentrating solar power (CSP) plants. However, their high corrosivity to commercial Fe-Cr-Ni alloys impedes the commercial applications of chloride-TES. In this work, we investigated the corrosion of two selected commercial Fe-based alloys (SS 310 and In 800H) in molten MgCl$_2$-KCl-NaCl salt, aiming to study the feasibility of affordable Fe-based alloys instead of expensive Ni-based alloys in the chloride-TES system. The alloy samples were immersed in the liquid-Mg-purified molten salt at 700 °C for 2000 hours under a protective inert gas atmosphere. After the corrosion test, SEM-EDX microstructural analysis and mass loss analysis showed that corrosion rates of the immersed alloy samples were lower than 15 μm/year, and the corrosion rates had a decreasing tendency with increasing immersion time during the 2000-hour test. To our best knowledge, this is the first experimental demonstration that corrosion rates of the Fe-based alloys in molten MgCl$_2$-KCl-NaCl salt at 700 °C can be controlled below the target (15 μm/year) proposed by the US Department of Energy (DOE). Using affordable Fe-based alloys as main structural materials, the cost of chloride-TES (27 USD/kWh) could be comparable to that of commercial nitrate-TES (20-33 USD/kWh). Taking advantage of chloride-TES with higher operating temperature, the next-generation CSP plant could use an advanced power cycle (e.g., sCO$_2$ Brayton) to have a much higher energy conversion efficiency, leading to a significantly lower Levelized Cost of Electricity (LCOE) than the current commercial CSP plant.

Keywords: Concentrating solar power (CSP), Thermal energy storage (TES), Fe-based alloy, Salt purification, Mg corrosion inhibitor.

---

[1] The short version of the paper was presented at ICAE2021, Nov 29 - Dec 5, 2021. This paper is a substantial extension of the short version of the conference paper.

1. INTRODUCTION

In order to use the advanced supercritical carbon dioxide Brayton power cycle with high thermal to electric energy conversion efficiency, next-generation (Gen3) concentrating solar power plants require operating temperatures above 700 °C for TES materials and heat transfer fluids (HTFs) [1, 2]. However, the nitrate salt mixtures (e.g., Solar Salt: $NaNO_3$-KNO_3 60-40 wt.%) for heat storage and transfer in the commercial CSP plants have limited operating temperatures of < 565 °C due to thermal decomposition [1, 3, 4]. Molten chlorides are promising high-temperature TES/HTF materials for the next-generation CSP plants due to high thermal stability (>800°C) and low cost [5-8]. In addition, the molten chloride coolant is of interest in the nuclear field for next-generation molten salt reactors (MSRs) [9-13]. Among the chloride salts, the $MgCl_2$-KCl-NaCl mixture is one of the most noticeable mixtures with the advantages of low melting point (~383 °C) [14], high thermal stability (stable above 800 °C) [7], low vapor pressure (~1 kPa at 800 °C) [7, 14, 15] and low cost (~0.22 USD/kg) [16]. In our previous work, eutectic $MgCl_2$-NaCl-KCl (47.1-30.2-22.7 mol.%, 56.5-22.2-21.3 wt.%) is recommended as one of the most promising compositions, satisfying both cost-effective and low-melting-point requirements [7, 17].

However, the compatibility issues, especially the severe corrosion of structural materials, make chloride salts challenging for high-temperature applications [1-2]. Molten unpurified $MgCl_2$-KCl-NaCl is strongly corrosive to Fe-Cr-Ni alloys even under a protective inert gas atmosphere [18-20]. Its strong corrosivity is mainly due to hydrolysis products, e.g., HCl and MgOHCl, formed during heating [15, 21-28]. More about corrosion mechanisms and behaviours of alloys in molten chlorides could be found in our previous review paper [18]. In contact with the unpurified molten chloride salts, few Fe-Cr-Ni alloy can reach the target corrosion rate (CR) of less than 15 μm/year at 700 °C. The CRs of Ni-based alloys in unpurified molten chloride salts are generally more than 100 μm/year at 700-800 °C, while CRs of Fe-based alloys (e.g., stainless steels) are even ten times higher than CRs of Ni-based alloys [13, 18, 29]. This CR-target of 15 μm/year was proposed by the US Department of Energy (DOE) to achieve a service life of at least thirty years for structural materials in next-generation CSP [30].

In addition to the high corrosivity of molten chlorides, the high costs of the Ni-based alloys limit their further application. The National Renewable Energy Laboratory (NREL) in the US estimated that if Haynes 230 (a commercial Ni-based alloy) is used as the main structural material of hot salt tank, the chloride-TES system would cost $58/kWh-th (US dollar per kWh in thermal), which is 2-3 times of that of the commercial nitrate-TES system ($20-33/kWh-th) [1]. Among the total estimated TES-cost, the cost of the hot tank is $41/kWh-th. It was pointed out that when stainless steel could be used as the main structural material of the hot tank, the cost of chloride-TES could be reduced to $27 /kWh-t. This cost would be similar to that of the commercial nitrate-TES [1].

Overall, a challenging but feasible way to achieve this cost target is to use Fe-based alloys as the main structural materials of chloride-TES under corrosion control.

One positive note is that the pure $MgCl_2$-KCl-NaCl mixture theoretically displays no spontaneous reactions (i.e., chemical corrosion) with Fe-Cr-Ni alloys even at high temperatures, based on thermodynamic data [31]. Hence, if the corrosive impurities, mainly MgOHCl, could be controlled at a low concentration level, the corrosivity of molten chloride salts to Fe-Cr-Ni alloys would be significantly mitigated [23, 29, 32-34]. A variety of methods have been explored to reduce the corrosive impurities in $MgCl_2$-containing chloride salts, including electrochemical methods [35, 36], thermal methods [15, 29, 37, 38], active-metal additive (e.g., Mg) [9, 15, 24, 32, 37-39], carbochlorination [9, 40, 41], and chlorination approaches [9, 42]. Among them , Mg-additive is regarded as a low-cost and powerful way for purification of industrial salts on the 30 000-metric-ton scale [9, 19, 38], which is in line with the amount of nitrate salt in commercial 100 MW CSP plants [1, 2]. In the previous work, with the removal of the main corrosive impurity MgOHCl by Mg addition, the CRs of some Ni-based alloys in $MgCl_2$-KCl(-NaCl) at >700 °C can be tens of microns per year, which is close to the DOE's target (CR < 15 µm/year) [24, 37, 39, 43]. The reaction of Mg with the main corrosive impurity in $MgCl_2$-KCl-NaCl is shown in **Eq. 1**.

$$Mg_{(s/l)} + 2\ MgOHCl_{(l)} \rightarrow 2\ MgO_{(s)} + MgCl_{2(l)} + H_{2(g)} \qquad \textbf{Eq. 1}$$
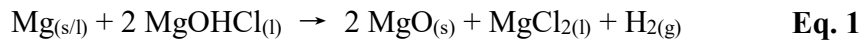
On the other hand, active metal (e.g., Mg) can play the role of a corrosion inhibitor in chloride-TES. According to Ellingham Diagram [9, 11, 31], the Mg metal is more reactive than the main alloying elements in the Fe-Cr-Ni alloy in molten chloride salts. Thus, it could act as the sacrificial anode and react with corrosive impurities generated during operation, such as MgOHCl, HCl, and Cl_2. Our previous work shows that equilibrium concentrations of Cr^{2+}, Fe^{2+}, and Ni^{2+} in molten $MgCl_2$-KCl-NaCl with excessive Mg are extremely low, with values of 2.3×10^{-10}, 1.5×10^{-12}, and 8.5×10^{-15} mol.% at 700°C, respectively [39]. In other words, the Fe-based alloys like stainless steels could theoretically exhibit acceptable low CRs in purified molten $MgCl_2$-KCl-NaCl with the Mg corrosion inhibitor.

Certain Fe-based alloys (particularly some austenitic steels) are of interest due to their relatively low costs and good high-temperature mechanical properties, which make them promising candidates structural materials at >700 °C [44-46]. Incoloy (In) 800H (1.4876) and stainless steel (SS) 310 (1.4845) are two commercial austenitic steels. Gilardi et al. reported that the cost of In 800H is about one-fourth of Ni-based alloys, while the cost of SS 310 is about the one-tenth cost of Ni-based alloys [47]. Therefore, if the CR of the Fe-based alloys in molten chloride salts can be controlled within the target (< 15 µm/year) by an affordable means, the cost of chloride-TES

will be comparable to the commercial nitrate-TES, benefitting from the fact that the material cost of chloride salts is about one-fifth of the cost of nitrate salts [1, 16].To our best knowledge, there is no literature experimentally demonstrating that a Fe-based alloy in $MgCl_2$-KCl-NaCl at 700 °C reaches the DOE's target (CR <15 µm/year [30]), although this is theoretically possible. In the available literature [15, 32, 39], lab-scale experiments show that CRs of stainless steel are still > 50 µm/year even with the addition of excessive Mg.

This work aims to investigate if the salt purification and corrosion inhibition method with Mg additive can control the CRs of the commercial Fe-based alloys in molten $MgCl_2$-KCl-NaCl at 700 °C to reach the DOE's target (CRs < 15 µm/year). Based on available literature and our previous work [15, 32, 39], the corrosion test procedure was optimized by immersing the steel samples in the molten salt purified with liquid Mg. The SS 310 (1.4845) and In 800H (1.4876) were immersed in $MgCl_2$-KCl-NaCl for up to 2000 hours (~2.8 months) at 700 °C with 2.8 wt.% Mg under an inert atmosphere. Then the corrosion behavior of these Fe-based alloys was characterized via different methods, including scanning electron microscope (SEM), Energy-dispersive X-ray spectroscopy (EDX), and X-ray diffraction analysis (XRD), as well as mass loss. Moreover, the impurity concentrations of the salt samples before/after the immersion tests were also analysed by acid-base titration and atomic absorption spectroscopy (AAS).

2. MATERIAL AND METHODS

2.1 Chemicals and alloys

Magnesium chloride ($MgCl_2$, Magnesia, purity > 99 wt.%), potassium chloride (KCl, Alfa Aesar, purity > 99 wt.%), and sodium chloride (NaCl, Alfa Aesar, purity > 99 wt.%) were weighed, mixed, and grinded in a glovebox (GS^{TM}, O_2<0.5 ppm, H_2O<1 ppm), to synthesize 300 g ternary eutectic $MgCl_2$-NaCl-KCl (47.1-30.2-22.7 mol.%) for the experiments [7]. Magnesium metal bars (purity > 99 %) with 5 mm diameter were cut, polished, and weighed as the additive.

Table 1 summarizes the chemical compositions of two tested commercial Fe-based alloys SS 310 (1.4845) and In 800H (1.4876). Before immersion, 10 × 10 × 2 mm SS 310 samples and 20 × 10 × 2 mm In 800H samples were polished successively with finer SiC sandpapers (600, 800, and 1200 grids) and washed with deionized water and dried with compressed air. Then the weight of each sample was recorded by an analytical balance with an accuracy of 0.0001g (i.e., 0.1 mg).

Table 1. Chemical compositions of the studied alloys (wt. %)

Alloy	Fe	Ni	Cr	C	Mn	Si	P	S	Al	Ti
SS 310	Bal.	19.00-22.00	24.00-26.00	0.25	2.00	1.50	0.045	0.030	-	-

In 800H	39.5	30.00-35.00	19.00-23.00	0.05-0.10	1.50	1.00	0.045	0.015	0.15-0.60	0.15-0.60
Data source: www.sandmeyersteel.com, access on February 9th of 2022										

2.2 Immersion tests

Fig. 1 shows the set-up sketch of the corrosion experiment. Six batches of 50 g chloride salt with 2.8 wt % Mg were produced in the glovebox by stoichiometric weighing into six separate alumina crucibles. The exposure time of the prepared salt in the air was less than 2 minutes to minimize the salt hydration during the transfer of salts from the glovebox to the test platform (autoclave). Then, the test platform was heated to 700 °C under an inert atmosphere (Ar 5.0: purity $\geqslant$ 99.999%, O_2 and H_2O < 1 ppm, flow rate: 10 L/h). After several-hour purification with liquid Mg (melting temperature of 650 °C) at 700 °C, a batch of salt samples was withdrawn from each of the six independent crucibles for post-analysis by acid-base direct titration to know their corrosive impurity levels. The six groups of alloy samples were then immersed into the purified molten salts in the six crucibles. As shown in Fig. 1, the alloy samples and nickel wire were separated by the insulating alumina tubes to prevent galvanic coupling due to direct contact between SS 310, In 800H, and the nickel wire. After 100, 250, 500, 1000, and 2000 hours of exposure, the alloy samples were extracted from the furnace and cleaned with distilled water. Upon taking each alloy sample from a crucible, the salt sample was subsequently withdrawn from the crucible and analysed by acid-based direct titration. The test conditions for different samples with specific sample identification (sample ID) are summarized in Table 2. The specific ID will be used throughout this work to denote the samples.

Table 2. Immersion corrosion test sample ID and corresponding test parameters.

Sample ID	Alloy	Duration of immersion hour	Sample size mm³	Test condition	CR method
SS310-100h	SS 310 (1.4845)	100	10 × 10 × 2	Immersion in 50 g MgCl₂-NaCl-KCl (47.1-30.2-22.7 mol.%, 56.5-22.2-21.3 wt.%) with 2.8 wt.% Mg additive at 700 °C under 10 L/h Ar 5.0 sweep gas.	SEM-EDX+ Mass loss
SS310-250h		250	10 × 10 × 2		SEM-EDX
SS310-500h		500	10 × 10 × 2		SEM-EDX
SS310-500h-2		500	10 × 10 × 2		Mass loss
SS310-1000h		1000	10 × 10 × 2		SEM-EDX
SS310-2000h		2000	10 × 10 × 2		SEM-EDX
In800H-100h	In 800H (1.4876)	100	20 × 10 × 2		SEM-EDX + Mass loss
In800H-250h		250	20 × 10 × 2		SEM-EDX
In800H-500h		500	20 × 10 × 2		SEM-EDX

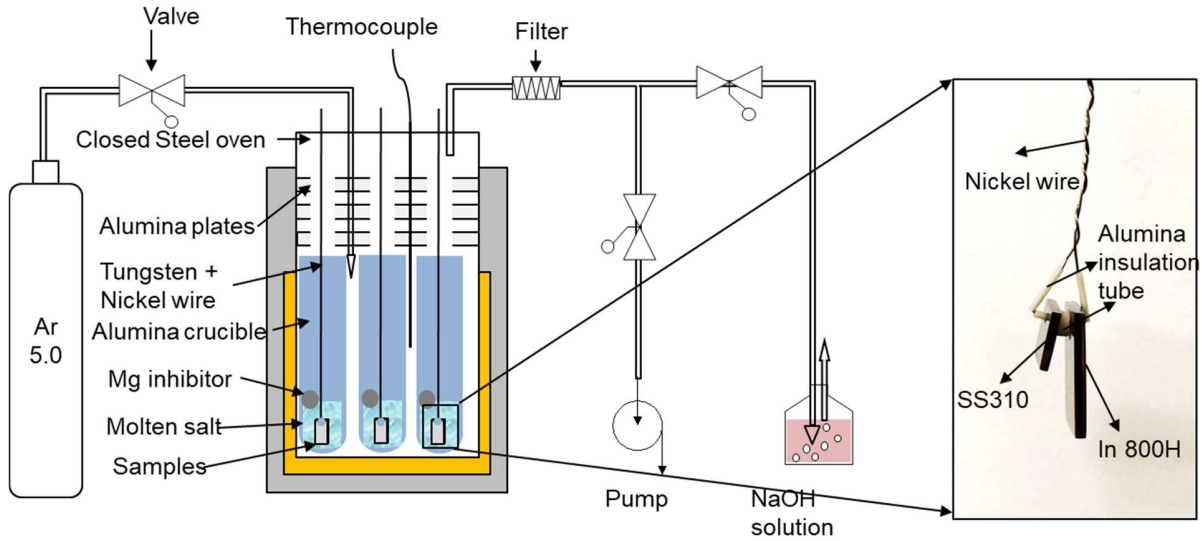|				
In 800H-500h-2	500	20 × 10 × 2		Mass loss
In800H-1000h	1000	20 × 10 × 2		SEM-EDX
In800H-2000h	2000	20 × 10 × 2		SEM-EDX

Fig. 1. Schematic diagram of experimental set-up for immersion test, and the sample holder with alloys samples.

2.3 Alloy corrosion analysis

Generally, the corrosion condition of an alloy can be quantitatively evaluated by corrosion rate (CR) with unit microns per year (µm/year). One method of calculating CR is based on the mass change of samples before/after the exposure tests [15, 18, 43, 48, 49]. Under the hypothesis of uniform corrosion, the CR is calculated as **Eq. 2** [48].

$$CR \ (\mu m/year) = \frac{K \times W}{A \times t \times \rho} \qquad \textbf{Eq. 2}$$

where,

K is a constant 8.76 ×10^7 (µm·h·cm^{-1}·year^{-1});

W is the mass loss of samples in g;

A is the sample's surface area in cm^2,

t is immersion time in hour; ρ is the density of samples (g/cm^3).

ρ is the density. The density of SS 310 and In 800H is 7.89 g/cm^3 and 7.95 g/cm^3, respectively.

Before the mass-loss measurement of this work, the oxide films on samples were washed away according to the standard ASTM-G1 [48]. In this work, mass loss method was carried out on Samples SS310-100h, In800H-100h, SS310-500h-2 and In800H-500h-2. However, the mass-loss measurement has two drawbacks that lead to a biased view of corrosion state of the samples. Firstly, it is pointed out that the acid-washing could also damage the alloy matrix and thus cause overestimation [48]. Secondly, the mass-loss method cannot characterize the non-uniform corrosion. For example, intergranular corrosion has a low mass-loss, but it can cause significant deep selective corrosion, resulting in material failure. Therefore, the macroscopic corrosion analysis (mass loss) should be combined with the microscopic analysis method, to reduce the misjudgment of the corrosion state of the samples.

In this work, the CRs of alloy samples were also evaluated by the microstructural analysis with Scanning Electron Microscopy (SEM, model: Zeiss LEO 1530 VP), equipped with Electron Dispersive X-ray spectroscopy (EDX). As shown in Table 2, SEM with EDX was the dominant method to investigate corrosion of samples. In order to maintain the maximum integrity of the samples (especially oxide film on surfaces), the SEM samples for mass loss tests were washed with deionized water except for the acid-washed 100h samples. As shown in Fig. 2, a 10-µm-thick-grid plot was put on the sample surface, divided into 1 µm x 1 µm small grids. The corroded grids (with the dark colour in SEM) were accounted for, while the CR was calculated according to Eq. 3 [23, 29, 39, 50].

$$CR \ (\mu m/year) = \frac{n_{cor}}{W_{SEM}} \times \frac{24 \times 365}{t} \qquad \textbf{Eq. 3}$$

where,

n_{cor} is the total number of corroded 1 µm x 1 µm grids;

W_{SEM} is the width of the SEM image in µm (e.g., 274 µm for Fig. 2);
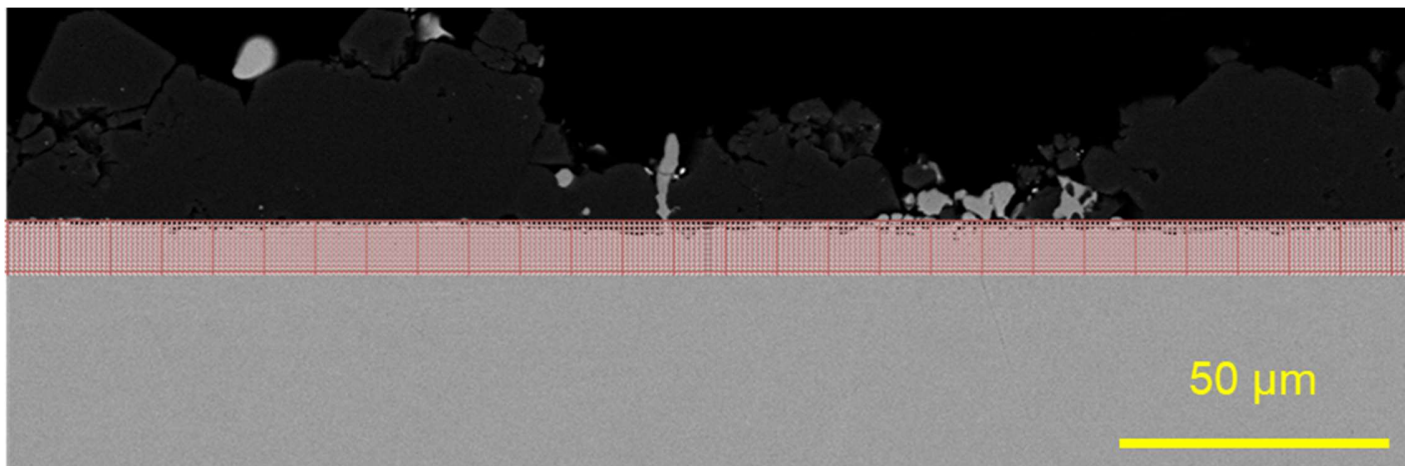
t is the immersion time in hour.

Fig. 2 Cross-section SEM image of SS 310-2000 h sample with grids for calculation of the corrosion rate.

A typical phenomenon of the corrosion layer of Fe-Cr-Ni alloy in molten chloride salt is the Cr-depletion since Cr is the most active metal among the main alloying elements of Fe, Ni, and Cr [15, 22, 29, 32]. Hence, the Cr-depletion is also available to describe corrosion of alloys in molten chloride salt. In order to determine the depletion of Cr in the corrosion layer, EDX-mapping was carried out to measure the main elements in the alloy.

The surface compositions of exposed samples were analysed by SEM-EDX and X-ray diffraction (XRD, Seifert PAD II) with Cu Kα1 radiation (λ = 0.15406nm, 40 kV, and 30 mA) in Bragg-Brentano geometry (θ-2θ) with a step size of 0.02˚ and a scan speed at 0.1˚/min.

2.4 Salts analysis with titration and AAS

Before and after immersion of alloy, 2-3 g molten chloride salt samples were extracted from each Alumina crucible. The acid-base titration was carried out to determine the concentration of corrosive impurities in experimental salts. It is well accepted that MgOHCl was the main corrosive impurity, as it has a high solubility in molten chloride salts [15, 18, 23, 29]. All the titrations were performed on the high-precision titration instrument 905 Titrando (Metrohm GmbH, Germany). The titers of the standard titrants (0.01 M HCl) (purchased from Merck KGaA, Germany) were validated with sodium carbonate (Na_2CO_3). About 500 mg salt sample was weighed and dissolved in 160 ml deionized water for each titration. During the titration, the N_2 sweep gas was employed to exclude the effect of carbon dioxide/carbonic acid. A 0.01 M HCl titrant was filled into the salt solution with an average 0.2 ml/minute rate. Simultaneously, a stirrer rotated continuously to make the solution homogeneous. A pH electrode measured the pH value of the salt solution. During titration, the pH value declined from ~9 to 4 with the filling of the HCl titrant. The HCl consumption at the equivalence point, where the amounts of acid and base were sufficient to cause complete neutralization, was recorded and used to calculate the impurity concentration. In order to obtain the mean value and standard deviation, each salt sample was titrated three times repeatedly. According to the consumption of 0.01 M HCl titrant at equivalence points, the concentration of the corrosive impurity MgOHCl with unit parts per million oxygen (ppm O) was calculated according to **Eq. 4**. The

unit ppm O is given to describe the proportion of the mass of the O-element in MgOHCl to the total sample mass [21, 51]. One hundred ppm O means 0.048 wt. % MgOHCl in samples.

$$C(MgOHCl)[ppm\ O] = C_{HCl} \times V_{HCl}/m_{sample} \times M_O \times 1000 \qquad \textbf{Eq. 4}$$

where,

V_{HCl} is the volume of HCl at equivalence point in L;

C_{HCl} is 0.01× titer in mol/L;

m_{sample} is the mass of the salt sample in g;

M_O is the molar mass of oxygen, i.e., 16 g/mol.

Moreover, the concentrations of Cr, Fe, and Ni elements in salt samples were measured with an atomic absorption spectrometer (AAS, Thermo Scientific iCE 3000 series, Thermo Fisher Scientific, US). A hollow cathode lamp was employed as the radiation source. The currents of the lamp were 12 mA for Cr and 10 mA for Fe and Ni. The analytical lines with a spectral bandwidth of 0.2 – 0.5 nm correspond to the Cr at 357.9 nm, the Fe at 248.3 nm, and the Ni at 232.0 nm. The operational software Solaar AA Version 11.03 was integrated into the spectrometer, which can be used for signal evaluation and concentration calculation. The standard solutions with the concentrations of 1, 2, and 5 mg/l for Cr, Fe, and Ni were prepared by dissolving the chloride or nitrate salt in 100 mL distilled water and adding 1 ml 1 wt.% HCl and 10 ml 10 wt.% CsCl solution. During the AAS tests for salt samples, about 1000 mg salt samples were dissolved in the 100 ml distilled water with 1 ml 1 wt.% HCl and 10 ml 10 wt.% CsCl. The procedure of AAS experiments was in line with that in our previous work [39]. To obtain a lower limit for AAS measurements, the amount of salt sample was ten times enlarged from 100 mg to 1000 mg. With this amount of salt samples, the measurement limits of AAS are 1.52 x 10^{-3} mol.% for Cr, 1.41 x 10^{-3} mol. % for Fe, and 1.35 x 10^{-3} mol.% for Ni, respectively.

2.5 Flowchart of the series experiments

Fig. 3 presents the flowchart of the series of experiments in this work. After exposure test, metal samples were cross-examined from both macroscopic (mass loss) and microscopic (SEM-EDX) perspectives. In parallel, corrosion impurity (MgOHCl) and corrosion products (e.g. Cr^{x+}, Fe^{x+}, Ni^{x+}) in the salt samples were also quantitatively analysed separately. Through such a series of experiments, the chance of experiments was reduced. The corrosion of metal samples and the corrosivity of salts were comprehensively evaluated.
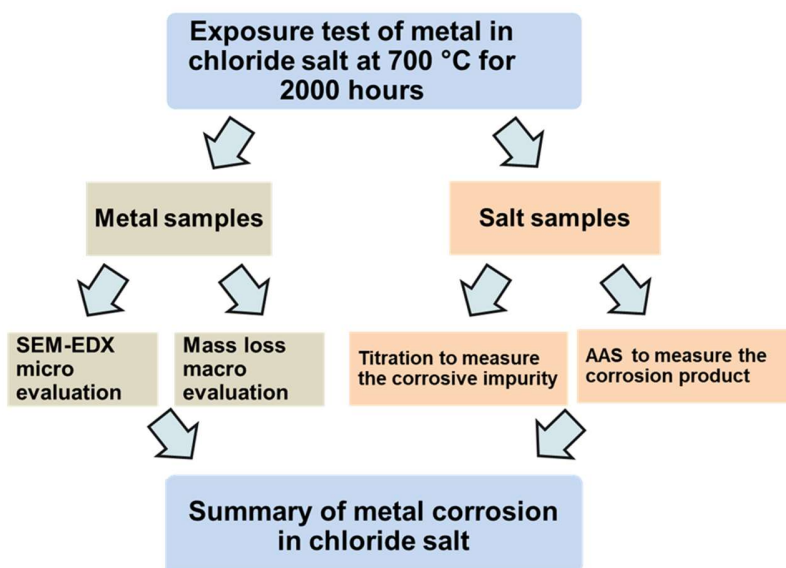
Fig. 3 Flowchart of the series experiments in this work. The corrosivity of salts and the corrosion of metal samples were evaluated separately.

3. RESULTS

3.1 Concentration of impurities in experimental salt

For evaluating the corrosivity of experimental molten chloride salts, the concentration of corrosive impurity MgOHCl in molten chloride salts in this work was determined by acid-base titration. After 16-hour pre-treatment with liquid Mg, i.e., before the immersion test of alloy samples, salt samples were extracted from each crucible. In addition, shortly after the exposure test of each alloy sample, the salt samples were extracted as well for post titration. Fig. 4 exhibits the concentration of the corrosive impurity (MgOHCl) in molten $MgCl_2$-KCl-NaCl mixtures before and after alloy immersion measured by titration, in which the error bars are the standard deviation of three-time titrations. In general, it can be concluded that the concentrations of MgOHCl in $MgCl_2$-KCl-NaCl mixtures purified with liquid Mg were lower than 200 ppm O (i.e., < 0.096 wt.%) during exposure testing of alloys.

The different operation durations could cause the fluctuation of MgOHCl concentration in sampling. A small amount of air inevitably diffused into the autoclave during the sampling. This leads to a reaction of the $MgCl_2$ with moisture in the leaked air, as shown in **Eq. 5**. The longer the sampling continued, the more MgOHCl was produced. The duration of sampling varied within one minute, resulting the inconsistent concentration of MgOHCl from 123.3 ppm O to 182.2 ppm O as shown in Fig. 3.
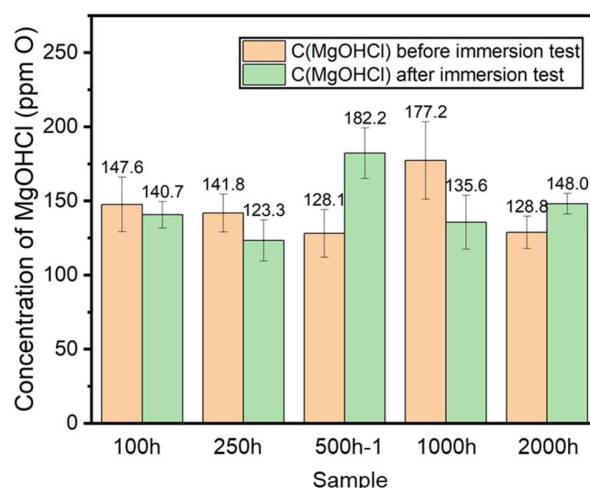
$$MgCl_2 \cdot H_2O_{(l/s)} \rightarrow \textbf{MgOHCl}_{(s)} + HCl_{(g)} \qquad \textbf{Eq. 5}$$
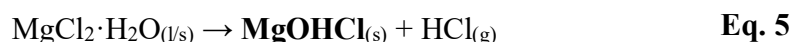
Fig. 4 Concentration of corrosive impurity MgOHCl in tested chloride salts before/after metal samples were immersed.

The concentrations of Cr, Fe, and Ni in all salt samples are smaller than their measurement limits of AAS, as shown in Fig. 5. In other words, the corrosion products in molten chloride salt are smaller than 1.52×10^{-3} mol.% after the 2000h corrosion test. Based on such low concentrations of MgOHCl and corrosion products in salt samples, it is believed that the corrosivity of the purified molten chloride salts was controlled successfully.
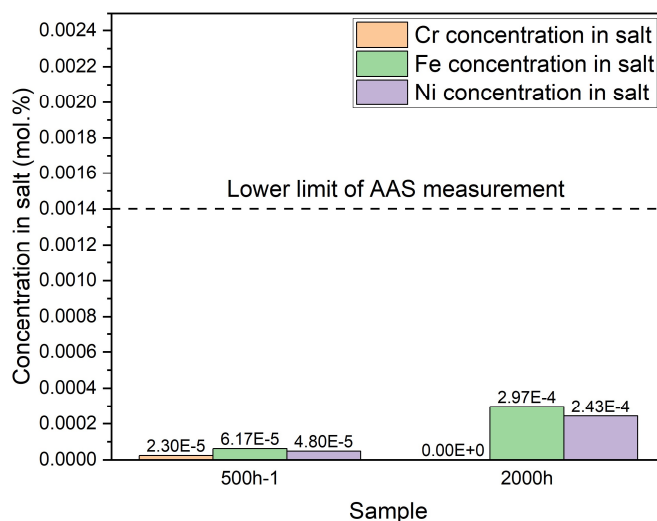
Fig. 5 The concentrations of Cr, Fe, and Ni in the molten chloride salt measured with AAS. The samples 500h-1 and 2000h mean the samples were extracted immediately after metal Samples-500h and -2000h, respectively. All the results are much lower than limit of AAS.

3.2 Surface characterization of exposed alloys

Fig. 6 shows the surface morphologies and the corrosion products of the exposed alloy samples. The optical pictures of the samples exposed for 250 h and 2000 h are shown in Fig. 6 (h). The sample exposed for 2000 h shows the black color, and its surface is covered with some particles. Fig. 6 (a) – (f) display the SEM images and corresponding EDX-mapping of Sample SS310-500h. Surface images of Sample SS310-500h show some tetrahedral crystal particles. According to the corresponding EDX-mapping, the particles are enriched in Mg and O, while the uncovered substrate shows a strong signal of Fe, Cr, and Ni, which are the dominant alloy elements of SS 310.

The phase compositions of the species on the surfaces of Samples SS310-1000h and In800H-1000h were examined by XRD, as shown in Fig. 6 (g). For both SS 310 and In 800H, the diffraction reflections of MgO at $2\theta=37.1°$, $42.6°$, and $62.5°$ are dominant. In addition, the austenite phase was detectable in the XRD patterns of both studied Fe-based alloys, which indicates the surfaces of both samples were not fully covered by oxide precipitations after 1000 h exposed to molten chloride salt. Moreover, the XRD pattern of the Sample SS310-1000h shows a slight signal of $MgCr_2O_4$. In contrast, no reflection of $MgCr_2O_4$ was detected on Sample In800H-1000h. Based on the SEM-EDX and XRD results, MgO is the dominant deposit on the surface of both SS 310 and In 800H. Fig. 7 shows the evolution of surface morphologies of SS 310 and In 800H samples during exposure to Mg-additive chloride salt for 2000 hours. After 250 h, small size MgO particles (size of < 3 μm) were aggregated on the surface of SS 310 and In 800H (Fig. 7 (a) and (e)), followed by MgO crystal particles with the size of tens of micrometre eventually covering the entire surface (Fig. 7 (d) and (h)). The growth process of MgO on SS 310 and In 800H samples was similar during the 2000h-immersion test.
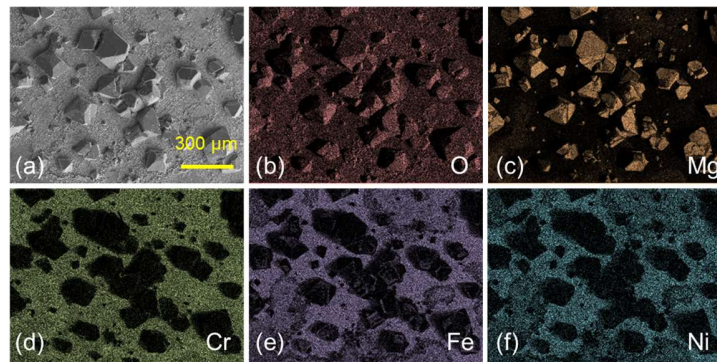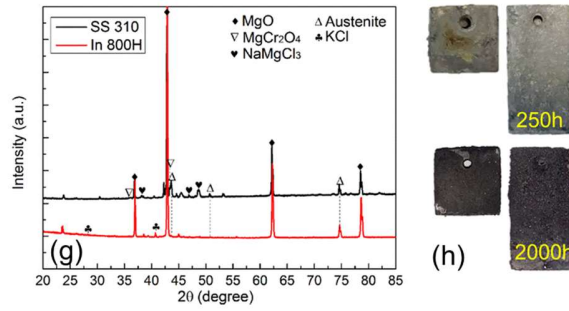
Fig. 6 (a) SEM image and (b)-(f) corresponding EDX-mappings of SS 310-500h sample surface. (g) XRD pattern of Samples SS310-1000h and In800H-1000h sample surfaces. (h) optical pictures of 250h and 2000h samples after test (SS 310: 10 × 10 × 2 mm, In 800H: 20 × 10 × 2 mm).
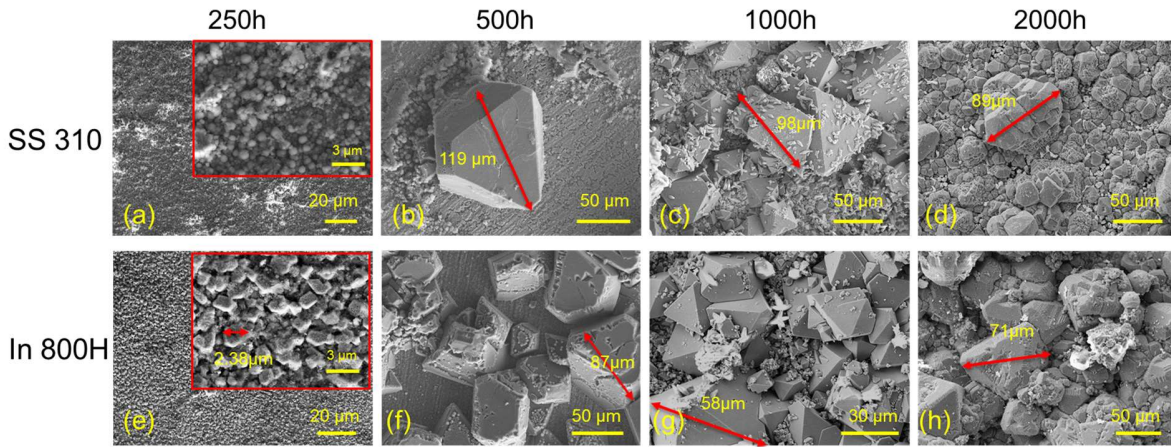

Fig. 7: Development of MgO morphology at the surface of metal samples during the 2000 hours exposure test in MgCl$_2$-KCl-NaCl at 700 °C under Ar, characterized by SEM.

3.3 Corrosion evolution of alloys in molten chloride salt

The mass losses of Samples SS310-100h and In800H-100h were recorded after descaling according to the ASTM-G1 standard [48]. As shown in Fig. 8 (a) and (e), no residual oxide layer can be observed on the surfaces of Samples SS 310-100h and In 800H-100h after descaling, confirming the acid washing can erase the oxide layer. According to the mass loss of Samples SS310-100h, In800H-100h, SS310-500h-2, and In800H-500h-2, the CRs$_{(mass-loss)}$ of the studied alloys are calculated based on Eq. 2. The CRs$_{(mass-loss)}$ of SS 310 are 52.6 ± 2.11 and 12.4 ± 0.38 µm/year for 100 hours and 500 hours, respectively, while CRs$_{(mass-loss)}$ of In 800H are 15.3 ± 2.11 and 5.3 ± 0.38 µm/year, respectively. The error here originates from the measurement limit of the balance.
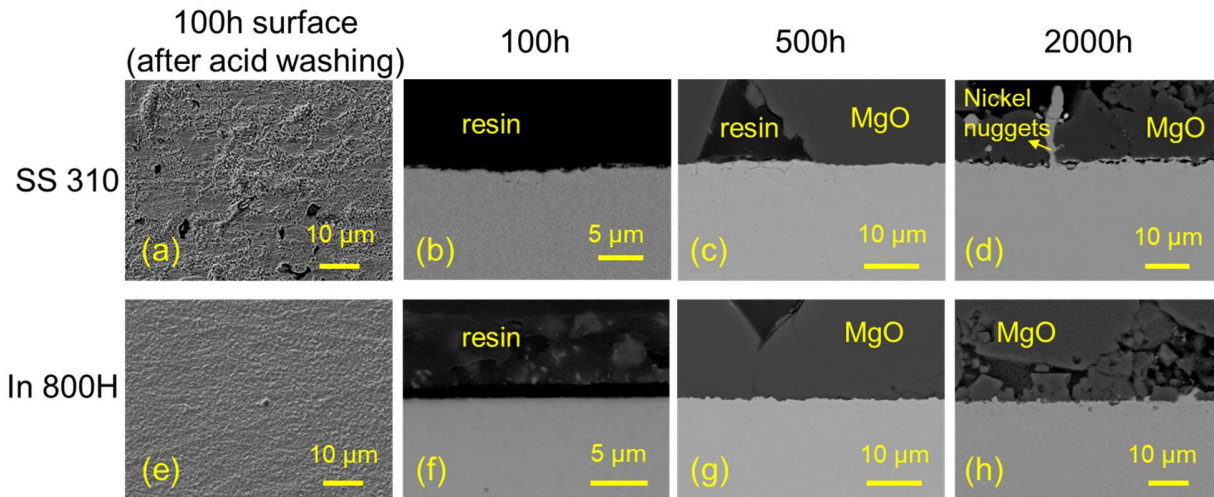
Fig. 8: Development of corrosion morphology of alloy samples during the 2000 hours exposure immersion test in MgCl₂-KCl-NaCl at 700 °C under Ar, characterized by SEM on their cross-sections.

Fig. 8 displays the development of corrosion morphology of tested samples during the 2000h-immersion test in the purified $MgCl_2$-KCl-NaCl molten salt at 700 °C under Ar sweep gas. On most of the SEM images, only thin corrosion layers can be observed. According to grid counting on SEM images mentioned in Eq. 3 and Fig. 2, the CRs of samples were calculated and summarized, as shown in Fig. 9. The corrosion depths of SS 310 and In 800H are notably small (1.73 ± 0.36 µm for SS 310 and 1.13 ± 0.5 µm for In 800H) after 2000-hour immersion, suggesting that CRs $_{(grid-counting)}$ are 7.6 ± 1.6 µm/year and 4.9 ± 2.2 µm/year of SS 310 and In 800H, respectively. The error here originates from the standard deviation of corrosion depth of three different parts for the same sample. Since the corrosion depth is limited, the position of the sample embedded in the resin and the initial surface roughness of the sample affected the CR calculation significantly, leading to high relative errors in CRs. Overall, the CRs from grid counting and mass loss are comparable under identical experimental conditions (see Fig. 9). The CRs of both SS 310 and In 800H show a decreasing tendency with increasing exposure time. For example, the CR of SS 310 decreases from ~53 µm/year to <10 µm/year with increasing immersion time from 100 hours to 2000 hours.
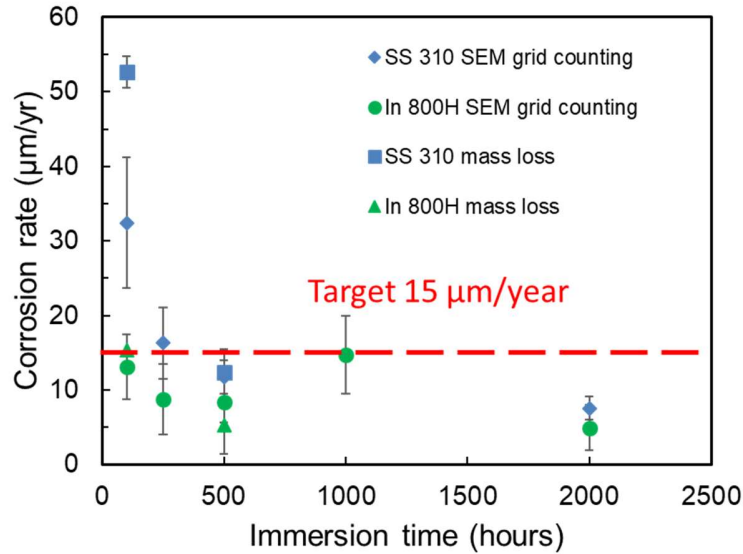
Fig. 9 Corrosion rates of SS 310 and In 800H based on SEM-grid-counting and mass loss results as a function of the immersion time.

Fig. 10 and Fig. 11 provide SEM images of 2000-hour-sample cross-sections and elemental analysis by EDX-mapping. As shown in Fig. 10 (a), a non-uniform MgO layer with a thickness of about 80 μm was observed on the surface of SS 310. The corrosion layer was almost invisible. The enlarged SEM image and EDX-mapping of the corrosion layer of SS 310 are shown in Fig. 10 (b)-(g). Some small holes with an average depth of 3 μm beneath the MgO layer were observed. From the EDX-mapping images, chromium distributes in the matrix unevenly. In addition, there exists some nickel enrichment at the surface of the sample and depletion in the matrix simultaneously.

For Sample In800H-2000h, some parts of its surface were also covered with MgO (as shown in Fig. 8 (h)), while another typical surface feature is covered with Ni enrichment (as shown in Fig. 11 (g)). In contrast to the nugget shape on Sample SS310-2000h, the Ni-enrichment on Sample In800H-2000h exhibits a relatively uniform and continuous layer. Besides Ni, few other matrix elements such as Fe and Cr were measured by EDX. Furthermore, the Cr distribution in Sample In800H-2000h is more uniform than that in Sample SS310-2000h. The corrosion layer is also barely visible on sample In800H-2000h and exhibits a thickness below 2 μm. For Samples SS310-2000h and In800H-2000h, no typical Cr-depletion layer was observed by EDX-mapping. Because the Cr-depletion is a typical feature of corroded Fe-Cr-Ni alloy in molten chloride salts [15, 29, 32], the little-Cr-depletion indicates that the corrosion on the 2000h-samples is slight.
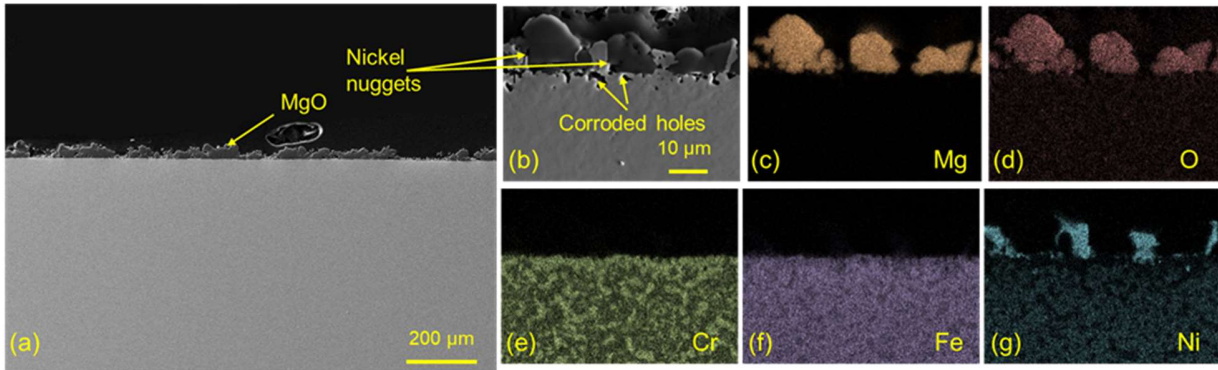
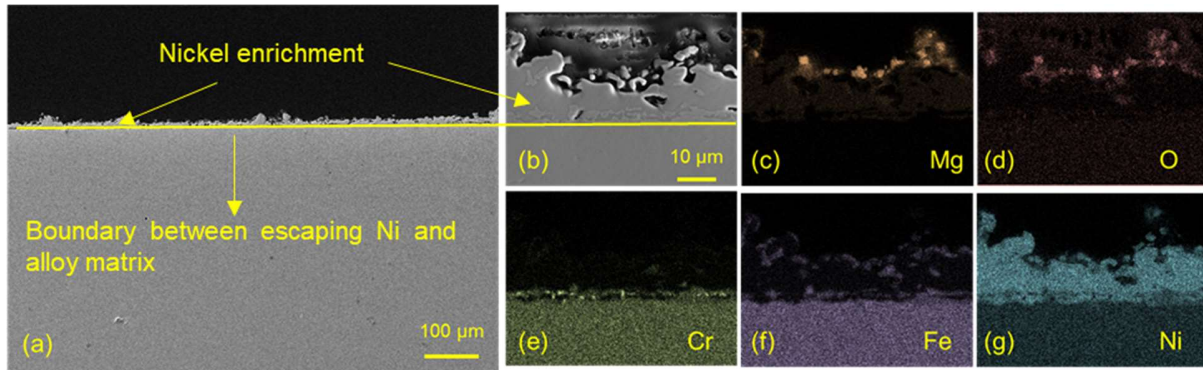**Fig. 10. Cross-section SEM and EDX-mapping images of Sample SS 310-2000h.**

Fig. 11. Cross-section SEM and EDX-mapping images of Sample In800H-2000h.

4. DISCUSSION

4.1 Development and Influence of MgO layer

It is reasonable to assume that there are two sources of MgO in the presented experiments, as discussed in our previous work [29]. On the one hand, formed MgO was originated from the spontaneous decomposition of MgOHCl, which was generated from the hydrolysis of hydrated $MgCl_2$ such as $MgCl_2 \cdot H_2O$, as shown in **Eq. 6** and **Eq. 6** [25, 27, 29]. On the other hand, both alloying elements in specimens (e.g., Cr) and metal Mg react with the dissolved MgOHCl impurity in the molten salt, leading to the formation of the MgO layer on the surface of samples, as shown in **Eq. 7**. It should be noted that Mg is the primary reactant (the M shown in **Eq. 7**), owing to the higher activity of Mg than that of Cr. Fe, and Ni [39]. In contrast to the previous work with a clear signal of $MgCr_2O_4$ [23, 29], a weak signal of $MgCr_2O_4$ was detected by XRD in this work, while no Cr signal was detected with EDX in the oxide layer, indicating that Cr-depletion was too little from the alloy to form Cr-rich oxide. The little Cr-rich oxide is a sidelight of the low-level corrosion in this work.

$$MgOHCl_{(s)} \;\rightarrow\; MgO_{(s)} + HCl_{(g)} \qquad\qquad \textbf{Eq. 6}$$

$$M_{(Mg, Fe, Cr, Ni)} + 2MgOHCl_{(l)} \rightarrow 2\mathbf{MgO}_{(s)} + MCl_2 + H_{2(g)} \qquad \textbf{Eq. 7}$$

As displayed in Fig. 7, the MgO grew gradually on the surface of samples during the 2000h-immersion test. It is foreseeable that without any actions, a dense MgO layer would also grow on the structural material in the future applications of chloride-TES. Although it makes sense in principle that a dense and continuous MgO layer could inhibit the attack of MgOHCl on the alloy by acting as a barrier, there is no direct evidence that the MgO layer on the alloy sample is dense enough to inhibit the attack of MgOHCl. In the previous work [23, 24, 29, 39] with significantly thick MgO layer, the corrosion layers in the matrix are still as high as tens of microns in molten chloride salt. In the present work, even for the same sample (e.g., Sample In800H-2000h), the distribution of the MgO layer is unevenly distributed. A part of the sample surface was covered by the MgO layer, as shown in Fig. 8 (h), while a part of the sample surface was covered by Ni-enrichment, as shown in Fig. 11 (a). However, the corrosion depth under these two types of surfaces is equally tiny, implying that the corrosion layer depth has no significant relationship with the MgO layer in this case. Moreover, blockages or performance drop caused by MgO in the cycle of chloride-TES might lead to high operating cost. Hence, the large particle and thick layer of MgO in the cycle of the system are potential risks. Filters reported in reference [15] can be employed to remove MgO particles out of the molten salt and solve such problems.

4.2 Corrosion of Fe-based alloys in molten chloride salt at 700 °C

The presented results experimentally prove that Fe-based alloys can reach the target of 15 μm/year proposed by DOE [30] in MgCl$_2$-KCl-NaCl mixtures at 700 °C with Mg salt-purifier and corrosion-inhibitor. Firstly, according to the corrosion results (Fig. 9), the CRs based on mass loss and microstructural analysis of 500-2000h samples are always smaller than 15 μm/year. Secondly, almost no Cr-depletion can be observed from EDX mapping, which confirms the low CRs of the alloy samples. In addition, the MgO is the dominant component of the oxide layer, while very weak Cr-enrich oxide was detected, which confirms again that the Cr-depletion from the matrix is small, i.e., the corrosion of alloy samples is slight. The target of 15 μm/year means that the corrosion depth of the primary structural material will be less than 0.5 mm, after 30 years of operation.

Fig. 12 shows the corrosion-depth development of the samples with different exposure times. As can be seen, the corrosion depth increases sharply in the first 100 hours of tests, while after 250 hours, the corrosion curve is relatively flat. The corrosion development of SS 310 and In 800H in molten chloride salt in this work is comparable to that of Inconel 600 used in fluoride loop in the literature [52] (Figure 12.1 in [52]). In the long-term corrosion test of the fluoride loop, the rapid corrosion of the first 250 hours is the initial impurity-driven corrosion. In comparison, the slow corrosion after 250 hours was a thermal gradient effect resulting from the metal solubility difference in molten fluoride salt at different temperatures and parts [52].

Although the corrosion curves of previous and this work are comparable, the explanations of corrosion in that dynamic fluoride loop and this static chloride test are not in line. There exists no thermal-gradient-effect corrosion in this static corrosion test. The impurities (e.g., MgOHCl) drove the corrosion of samples in this work. As shown in Fig. 4, the concentration of the main corrosive impurity MgOHCl was at a similar level, i.e., < 200 ppm O in separate crucibles after various exposure times. Hence, it is probable that the variation of CRs is not attributed to the concentration difference of MgOHCl. A possible cause of the relatively high mass loss in the early stage could be the rapid passivation of the bare metal after polishing. After that, corrosion would be controlled by diffusion of the alloying elements involved in the corrosion reactions, which was slower.
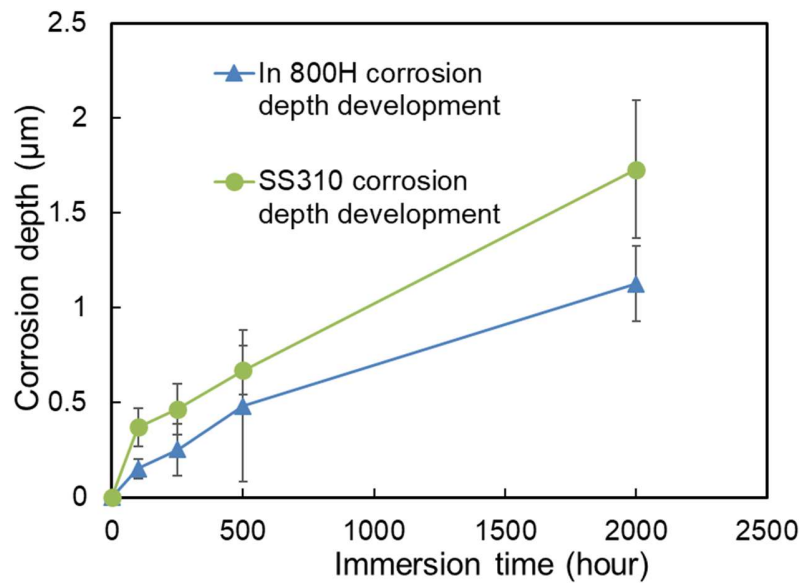

Fig. 12. SS 310 and In 800H corrosion development in MgCl$_2$-KCl-NaCl at 700 °C under Ar sweep gas. The salts were purified with 2.8 wt.% Mg at 700 °C for 16 hours before tests.

The estimated CRs of alloy in molten chloride salt in this work are low, however, the problem of Ni-enrichment on the surface is noteworthy, as shown in the EDX-mapping of Samples SS310-2000h and In800H-2000h (i.e., Fig. 10 (g) and Fig. 11 (g)). This phenomenon is particularly evident in the Sample In800H-2000h, which shows a continuous Ni-enrichment layer with a height of 20 μm. One plausible explanation for this is that the Ni in the sample matrix has a high affinity with the Mg metal dissolved in molten chloride salt. The Mg-Ni interaction phenomenon was also observed by other researchers in corrosion tests of Fe-Cr-Ni alloys with Mg-rich molten chloride salts [22, 43, 53]. The research on Mg-Ni interaction is insufficient and requires further investigation.

Another noteworthy point from EDX-mapping is inhomogeneous Cr-distribution in SS 310 after 2000h exposure to molten salt at 700 °C, as shown in Fig. 10 (e). This inhomogeneity is not due to the impact of molten chloride but the segregation of Cr in SS 310 at 700 °C. The following two reasons are given to support this view.

Firstly, the inhomogeneous Cr distribution in SS 310 after 2000h exposure is observed not only near the surface but also in the deep matrix (see Fig. 13). In the deep matrix that was inaccessible to the melts, only high temperature can affect the distribution of Cr. Secondly, in literature [54, 55], the austenitic stainless steels were tested/in service at temperatures above 600 °C without molten salt. In these cases, Cr-rich secondary phases, such as the sigma phase, were presented at grain boundaries (GBs), leading to the inhomogeneous Cr distribution. The embrittle sigma phase precipitates at GBs, leading to the degradation of these steels' mechanical properties (especially anti-creep property) at high temperatures [56], indicating that the 700 °C seems not the optimum service temperature of SS 310. For the future application of chloride-TES tank, stainless steels with better thermal stability at >700 °C are required, which should have reasonably high-temperature mechanical properties, especially anti-creep properties [57].
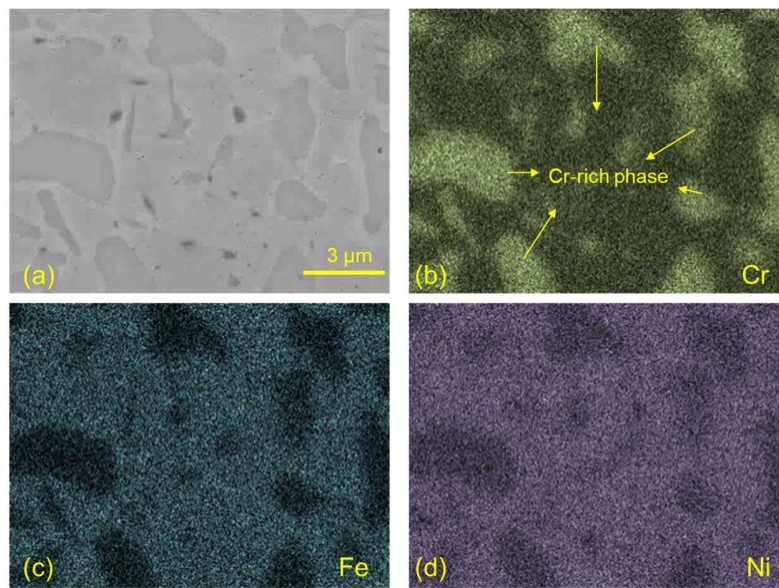

Fig. 13. SEM and EDX-mapping images of Sample SS 310-2000h in the deep matrix. Cr-rich phase is observed.

4.3 Influence of purification methods on CRs of Fe-based alloys

The purification method is essential for the corrosion control. It was pointed out that the corrosion products can accelerate the corrosion of metal matrix in molten chloride salt [28]. For example, the corrosion product Cr^{3+} can oxide the Cr in alloy to Cr^{2+}. Some similar conclusions have also been drawn in the field of molten fluoride salt [11]. Hence, the discussion of purification strategies is necessary.

Table 3 summarizes the CRs of Fe-based alloys in $MgCl_2$-containing molten salt at 700 °C under an inert atmosphere, including the results from the Chinese Academy of Sciences (CAS) [32], the Oak Ridge National Laboratory (ORNL) [40], our previous work [29, 39], and this work. All the molten chloride salts were chemically

purified, except for the molten chloride salts employed in ref. [29] not purified with any chemical methods as a reference, in which the CR of SS 310 is as high as 1752 μm/year.

Table 3 Comparison of CRs for Fe-based alloys in MgCl$_2$-containing molten salt at 700 °C under inert atmosphere.

Materials	Purification method	Immersion time hour	Salts	CR based on mass loss μm/year	CR based on SEM-EDX μm/year	Data sources
SS 310	-	500	MgCl$_2$-KCl-NaCl	1581[a]	1752	DLR [29]
In 800H				364[a]	876	
SS 310	Adding 1 wt.% Mg			-	298	DLR [39]
In 800H				-	262	
SS 310	Salt pre-treatment by 2.8 wt.% liquid Mg + test with excessive Mg	500		12.4[a]	~12[b]	This work
In 800H				5.3[a]	~8[b]	
SS 316	Salt pre-treatment by solid Mg and test with 1 wt. % Mg	400		51	~ 20 μm corrosion along grain boundary after 400-hour test	CAS [32]
SS 316 (carburized)				52	~ 60 μm corrosion along grain boundary after 400-hour test	
SS 316	Salt dried at 300 °C for 24 hours	100		261	~ 50 μm corrosion along grain boundary after 100-hour test	CAS [20]
SS 316 L	Salt pre-treatment by CCl$_4$ bubbling	100	MgCl$_2$-KCl	18	almost invisible	ORNL [35]
a. For mass loss measurement, the samples were washed by acid according to ASTM G1 [48].						
b. Errors of these values are high because of almost invisible corrosion layers on samples, as shown in Fig. 8 (c), (g) and Fig. 14 (c).						

Kurley et al. from ORNL purified 600g MgCl$_2$-KCl salt with CCl$_4$ bubbling at 850 °C for over 100 hours [40]. Then SS 316 L samples were immersed in purified salt for 100 hours at 700 °C. Based on mass loss, the CR of SS 316 L was about 18 μm/year in this case, implying that intensely chemical pre-treatment is an effective method to decline the corrosivity of molten chloride. However, due to its expensive cost and toxicity, the CCl$_4$ bubbling method could be challenging for large-scale purification and application.

In our previous work [39], Mg (1 wt.%) was used as the additive to mitigate molten chloride salt corrosion of alloy samples. During the heating, some produced corrosive impurities like MgOHCl and HCl, before reacting

with Mg, corroded the SS 310 sample, leading to a 17 μm corrosion layer in 500 hours immersion test (298 μm/year) [39]. Ren et al. in CAS used a Mg rod to purify $MgCl_2$-KCl-NaCl at 600 °C for 24 hours [32]. After purification, standard SS 316 and carburized SS 316 samples were immersed into purified salt with 1 wt. % Mg for 400 hours at 700 °C. Although the mass loss results imply that the CRs of samples were not severe (~51 μm/year), the corrosion depth at the cross-section measured by SEM was relatively high due to intergranular corrosion. The passivation of the Mg rod by the MgO layer (see **Eq. 1**) could result in the corrosive impurities were not reduced to a low level, leading to relatively large intergranular corrosions.

As shown in **Fig. 14**, sketches of three corrosion experiments performed at the German Aerospace Center (DLR) are summarized. In this work, the alloy samples were immersed in molten chloride salts at 700 °C, pretreated by 2.8 wt. % liquid Mg for 16 hours. With this approach, the concentration of MgOHCl in this work is controlled under 200 ppm O, while the concentrations of Cr, Fe, and Ni were smaller than 1.52 x 10^{-3} mol.% in melts, resulting in the CRs being smaller than 15 μm/year. Furthermore, with a suitable corrosion inhibitor, the CR decreases with the increasing test time, as shown in Fig. 9.

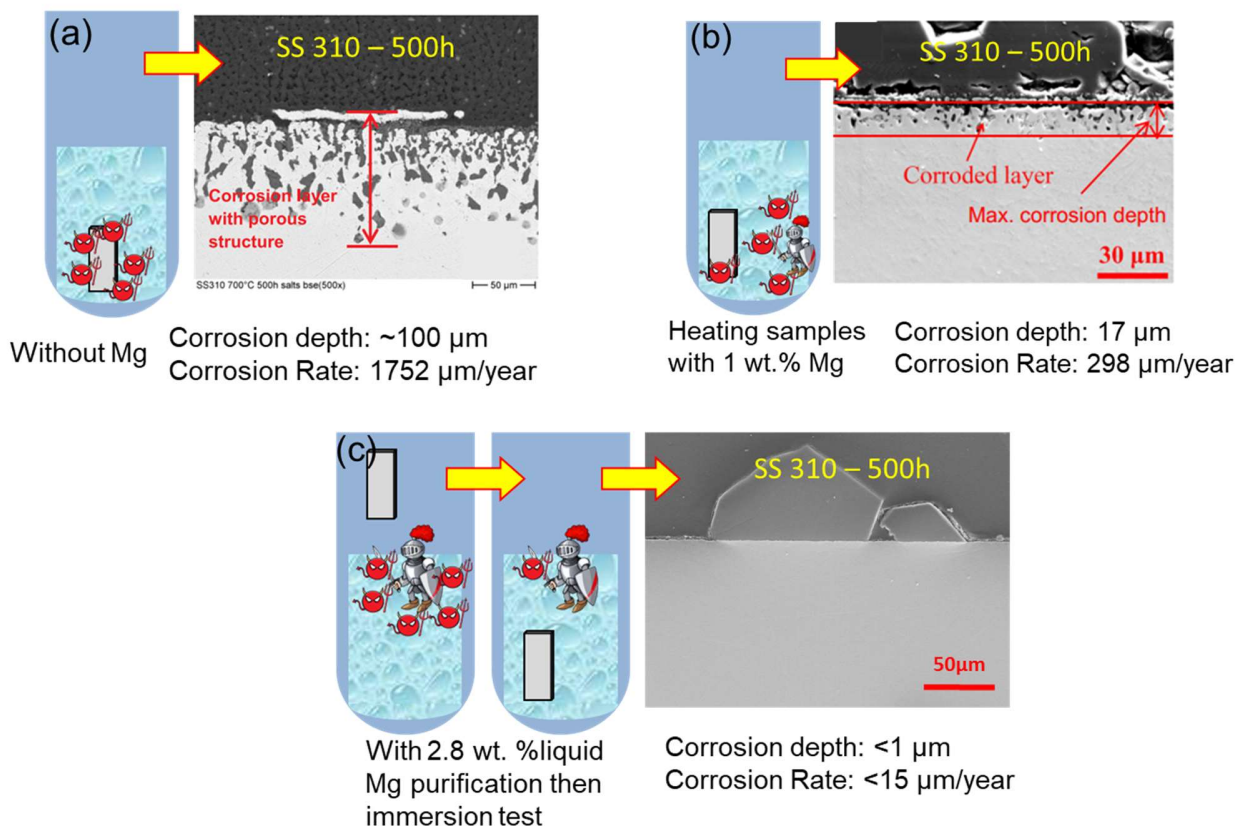**Fig. 14. Comparison of three exposure tests at DLR. The tests were performed at the same platform with $MgCl_2$-KCl-NaCl at 700 °C under Ar sweep gas. (a) SS 310 was heated with the impurified salt to 700 °C and held for 500 hours [29]; (b) SS 310 was heated with salt and 1 wt.% Mg to 700 °C and held for 500**

hours [39]. (c) In this work, the salt was purified with 2.8 wt.% liquid Mg at 700 °C for 16 hours, and then the SS 310 was immersed in purified salt. Red devil: MgOHCl; Knight: Mg metal.

According to the experience learned from this work, an industrial procedure similar as that for the commercial molten nitrate-TES system could be designed for the molten chloride-TES system, as schematically shown in Fig. 15. Based on the promising salt purification effectiveness of Mg in this work, an equipment (similar as the commercial pre-melting equipment for nitrate salts [58]) is patented [59] and will be developed for pre-melting and salt purification with Mg. After pre-melting and salt purification, the molten chloride salt will be pumped to the commercial salt tank of the CSP plant. During the operation of the CSP plant, the molten chloride flows in the molten chloride TES system. The corrosion control system (CCS) in the chloride-TES is necessary for the 30-year service life of CSP [7]. The CCS consists of two parts: corrosion monitoring and corrosion mitigation. In this work, the corrosion monitoring part corresponds to the titration and AAS methods, giving ex-situ analysis of the salt corrosivity (e.g. MgOHCl concentration) and corrosion products. Besides the ex-situ analysis, some in-situ techniques based on some electrochemical methods (e.g., CV [21, 60, 61] and OCP [61]) could be used for online monitoring. In this work, the Mg metal plays two roles as both salt purifier before metal exposure and corrosion inhibitor during the 2000-hour test. In other words, the Mg metal could be also used as a corrosion inhibitor in CCS for corrosion mitigation. Except for Mg-inhibitor, other options such as electrolysis [36] could be used for corrosion mitigation. With the procedure described in Fig. 15 based on the promising results of this work, the corrosion rate of stainless steel in chloride-TES for commercial application in CSP could be controlled at a low level. However, static experiments on a laboratory scale cannot fully reflect the real situation in the industry. Therefore, subsequent study closes to the real conditions of CSP based on dynamic platforms is necessary for reducing the scaling-up risk of chloride-TES.
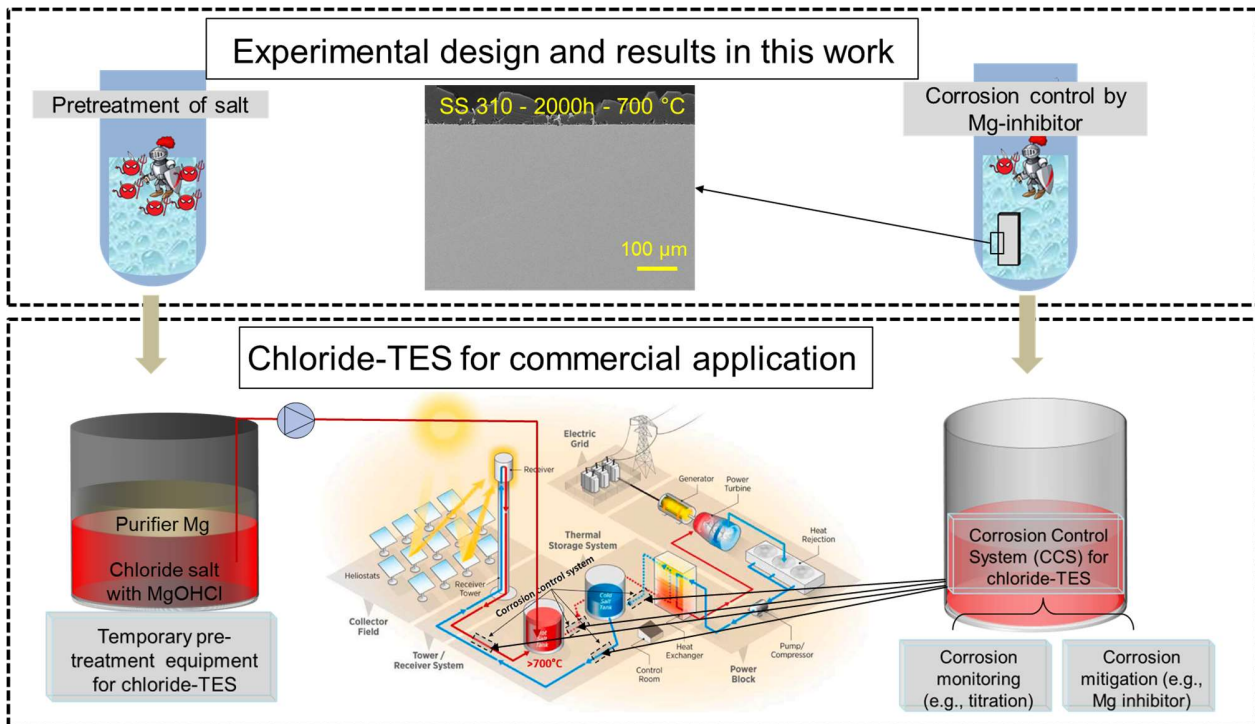
Fig. 15. Industrial procedure of chloride-TES for commercial application in CSP designed based on the results in this work.

4.4 Economic discussion on the chloride-TES

The corrosion of molten chloride salt to Fe-Cr-Ni alloy has long been one of the most challenging issues for molten chloride salt [1, 18, 20, 43, 62]. It is the prerequisite for the application of molten chloride salts to overcome the high corrosivity with a cost-effective approach, especially for the next-generation CSP with up to 30000-ton salt. In this work, we purified the inexpensive salt ($MgCl_2$-KCl-NaCl) with an inexpensive method (Mg-additive), controlling the corrosion rates of inexpensive alloys (Fe-based alloys) under 15 μm/year in molten chloride salt at 700 °C for 2000 hours.

The positive results of the static corrosion test suggest that stainless steel is a promising candidate for structural material for chloride-TES, which is in line with the main structural material for commercial nitrate-TES. Fig. 16 shows the cost comparison of nitrate- and chloride-TES. Among them, the costs of Nitrate-TES-1 (commercial case: Abengoa GO 18149, 20 $/kwh-th), Nitrate-TES-2 (commercial case: WorleyParsons, 33 $/kwh-th), and Chloride-TES-Ha 230 (estimation, 58 $/kwh-th) are available in the report published by the NREL [1], while the cost of Chloride-TES-SS (27 $/kwh-th) is estimated based on stainless-steel hot tank and $MgCl_2$-KCl-NaCl ternary chloride salt using the estimation model in the report of NREL. As can be seen, the stainless-steel hot tank leads to a sharply decreasing chloride-TES cost, resulting in a comparable cost with commercial cases of nitrate-TES.
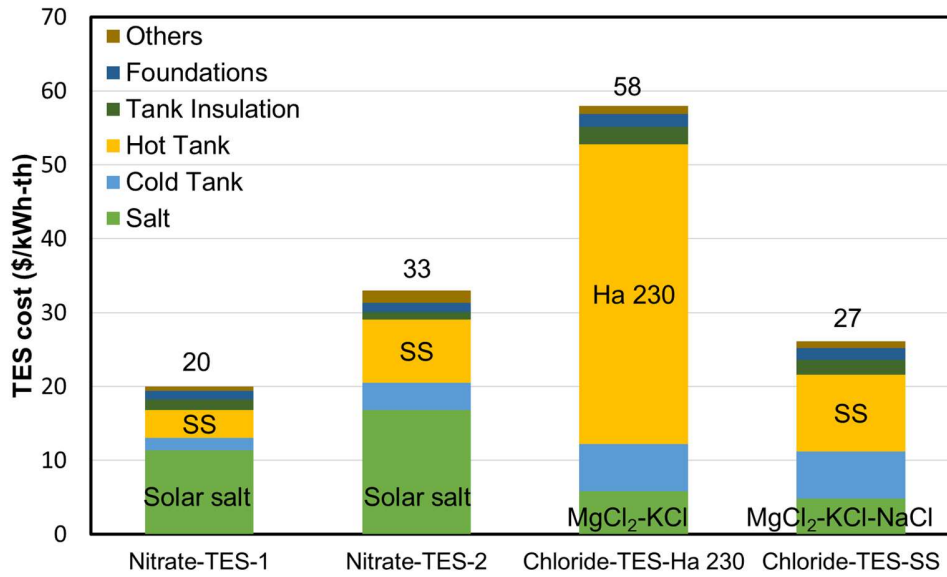
Fig. 16 A comparison of cost of commercial nitrate-TES with estimated chloride-TES [1]. When the stainless steel could be available in chloride-TES, the cost of chloride-TES would be in line with nitrate-TES.

5. CONCLUSIONS AND OUTLOOK

The main conclusions of this work are summarized as follows:

- Based on the 2000-hour exposure test, the corrosion rates of In 800H and SS 310 in the molten $MgCl_2$-KCl-NaCl salt purified with liquid Mg at 700 °C under the Ar atmosphere were 7.6 ± 1.6 μm/year and 4.9 ± 2.2 μm/year, respectively.

- The CRs of SS 310 in this work decrease from 52.6 μm/year to 7.6 μm/year, while CRs of In 800H decrease from 15.3 μm/year to 4.9 μm/year with increasing exposure time from 100 hours to 2000 hours.

- With an optimizing salt purification by 2.8 wt.% Mg before immersion tests, the concentration of MgOHCl corrosive impurity was smaller than 200 ppm O (~0.096 wt.%), which can be seen as the acceptable impurity level of $MgCl_2$-KCl-NaCl for Fe-based alloy.

- The development of oxide layers on the sample surface illustrated the growth of MgO particles from several micro-meter to be about one hundred micro-meters during the 2000-hour test. The MgO layers showed no apparent correlation with the corrosion depth in this work.

- An industrial procedure similar as that for the commercial molten nitrate-TES system could be designed for the commercial molten chloride-TES system to ensure the long service life time. It includes the salt pre-melting and salt purification by an equipment using Mg, pumping of the purified

salt into the commercial salt tank and corrosion control during the operation of the chloride-TES system by a corrosion control system.

In summary, this work experimentally proves that Fe-based alloys can reach the target of 15 μm/year proposed by DOE in MgCl₂-KCl-NaCl mixtures at 700 °C with Mg salt-purifier and corrosion-inhibitor. Moreover, if the stainless steels fulfill other essential requirements like mechanical properties, they can be used as the main structural material of the salt tank. This makes the chloride-TES system have a similar cost (27 USD/kWh-th) to the commercial nitrate-TES system and be more cost-effective and competitive.

In the future, the following work is suggested to develop the chloride-TES technology for final commercial applications:

- With Mg-additive, some stainless steels or Fe-based alloys with good high-temperature mechanical properties could be tested in molten chloride salt.

- Some essential structural elements (e.g., welding joint) could be tested in the purified molten chloride salt.

ACKNOWLEDGEMENT

REFERENCE

[1] Mehos M, Turchi C, Vidal J, Wagner M, Ma Z, Ho C, et al. Concentrating solar power Gen3 demonstration roadmap. United States: National Renewable Energy Lab.(NREL), Golden, CO (United States); 2017.https://doi.org/10.2172/1338899

[2] Ding W, Bauer T. Progress in Research and Development of Molten Chloride Salt Technology for Next Generation Concentrated Solar Power Plants. Engineering. 2021.https://doi.org/10.1016/j.eng.2020.06.027

[3] Bauer T, Odenthal C, Bonk A. Molten Salt Storage for Power Generation. Chemie Ingenieur Technik 2021;93:534-46.https://doi.org/10.1002/cite.202000137

[4] Villada C, Bonk A, Bauer T, Bolívar F. High-temperature stability of nitrate/nitrite molten salt mixtures under different atmospheres. Applied Energy. 2018;226:107-15.https://doi.org/10.1016/j.apenergy.2018.05.101

[5] Wei X, Song M, Wang W, Ding J, Yang J. Design and thermal properties of a novel ternary chloride eutectics for high-temperature solar energy storage. Applied Energy. 2015;156:306-10.https://doi.org/10.1016/j.apenergy.2015.07.022

[6] Vignarooban K, Pugazhendhi P, Tucker C, Gervasio D, Kannan AM. Corrosion resistance of Hastelloys in molten metal-chloride heat-transfer fluids for concentrating solar power applications. Solar Energy. 2014;103:62-9.https://doi.org/10.1016/j.solener.2014.02.002

[7] Villada C, Ding W, Bonk A, Bauer T. Engineering molten MgCl2–KCl–NaCl salt for high-temperature thermal energy storage: Review on salt properties and corrosion control strategies. Solar Energy Materials and Solar Cells. 2021;232:111344.https://doi.org/10.1016/j.solmat.2021.111344

[8] Vignarooban K, Xu X, Arvay A, Hsu K, Kannan AM. Heat transfer fluids for concentrating solar power systems – A review. Applied Energy. 2015;146:383-96.https://doi.org/10.1016/j.apenergy.2015.01.125

[9] Ambrosek JW. Molten chloride salts for heat transfer in nuclear systems: The University of Wisconsin - Madison; 2011.https://www.proquest.com/docview/885007950?parentSessionId=5Ny2J3Dfp0LfvlEPUHP6b3HyR2nnutVr4yPpB7p7OEY%3D

[10] Ezell NDB, Raiman SS, Kurley JM, McDuffee J. Neutron irradiation of alloy N and 316L stainless steel in contact with a molten chloride salt. Nuclear Engineering and Technology. 2021;53:920-6.https://doi.org/10.1016/j.net.2020.07.042

[11] Guo S, Zhang J, Wu W, Zhou W. Corrosion in the molten fluoride and chloride salts and materials development for nuclear applications. Progress in Materials Science. 2018;97:448-87.https://doi.org/10.1016/j.pmatsci.2018.05.003

[12] Raiman SS, Mayes RT, Kurley JM, Parrish R, Vogli E. Amorphous and partially-amorphous metal coatings for corrosion resistance in molten chloride salt. Solar Energy Materials and Solar Cells. 2019;201:110028.https://doi.org/10.1016/j.solmat.2019.110028

[13] Raiman SS, Lee S. Aggregation and data analysis of corrosion studies in molten chloride and fluoride salts. Journal of Nuclear Materials. 2018;511:523-35.https://doi.org/10.1016/j.jnucmat.2018.07.036

[14] Mohan G, Venkataraman M, Gomez-Vidal J, Coventry J. Assessment of a novel ternary eutectic chloride salt for next generation high-temperature sensible heat storage. Energy Conversion and Management. 2018;167:156-64.https://doi.org/10.1016/j.enconman.2018.04.100

[15] Zhao Y. Molten Chloride Thermophysical Properties, Chemical Optimization, and Purification. National Renewable Energy Lab.(NREL), Golden, CO (United States); 2020.https://www.osti.gov/biblio/1734652

[16] Turchi CS, Vidal J, Bauer M. Molten salt power towers operating at 600–650 C: Salt selection and cost benefits. Solar Energy. 2018;164:38-46.https://doi.org/10.1016/j.solener.2018.01.063

[17] Villada C, Ding W, Bonk A, Bauer T. Simulation-Assisted Determination of the Minimum Melting Temperature Composition of MgCl2–KCl–NaCl Salt Mixture for Next-Generation Molten Salt Thermal Energy Storage. Frontiers in Energy Research. 2022;10.https://doi.org/10.3389/fenrg.2022.809663

[18] Ding W, Bonk A, Bauer T. Corrosion behavior of metallic alloys in molten chloride salts for thermal energy storage in concentrated solar power plants: A review. Frontiers of Chemical Science Engineering. 2018;12:564-76.https://10.1007/s11705-018-1720-0

[19] Turchi C, Gage S, Martinek J, Jape S, Armijo K, Coventry J, et al. CSP Gen3: Liquid-Phase Pathway to SunShot. National Renewable Energy Lab.(NREL), Golden, CO (United States); 2021.https://doi.org/10.2172/1807668

[20] Sun H, Wang J, Li Z, Zhang P, Su X. Corrosion behavior of 316SS and Ni-based alloys in a ternary NaCl-KCl-MgCl2 molten salt. Solar Energy. 2018;171:320-9.https://doi.org/10.1016/j.solener.2018.06.094

[21] Ding W, Bonk A, Gussone J, Bauer T. Electrochemical measurement of corrosive impurities in molten chlorides for thermal energy storage. Journal of Energy Storage. 2018;15:408-14.https://doi.org/10.1016/j.est.2017.12.007

[22] D'Souza B, Zhuo W, Yang Q, Leong A, Zhang J. Impurity driven corrosion behavior of HAYNES® 230® alloy in molten chloride Salt. Corrosion Science. 2021;187:109483.https://doi.org/10.1016/j.corsci.2021.109483

[23] Grégoire B, Oskay C, Meißner T, Galetz M. Corrosion mechanisms of ferritic-martensitic P91 steel and Inconel 600 nickel-based alloy in molten chlorides. Part II: NaCl-KCl-MgCl2 ternary system. Solar Energy Materials and Solar Cells. 2020;216:110675.https://doi.org/10.1016/j.solmat.2020.110675

[24] Sun H, Wang J-Q, Tang Z, Liu Y, Wang C. Assessment of effects of Mg treatment on corrosivity of molten NaCl-KCl-MgCl2 salt with Raman and Infrared spectra. Corrosion Science. 2020;164:108350.https://doi.org/10.1016/j.corsci.2019.108350

[25] Kipouros GJ, Sadoway DR. A thermochemical analysis of the production of anhydrous MgCl2. Journal of Light Metals. 2001;1:111-7.https://doi.org/10.1016/S1471-5317(01)00004-9

[26] Kashani-Nejad S, Ng K, Harris R. Properties of MgOHCl. Metallurgical and Materials Transactions B 2004;35:406-8.https://doi.org/10.1007/s11663-004-0043-3

[27] Kashani-Nejad S. Oxides in the dehydration of magnesium chloride hexahydrate: McGill University; 2005.https://escholarship.mcgill.ca/concern/theses/ws859g01q

[28] Garcia-Diaz B, Martinez-Rodriguez M. Full loop thermodynamic corrosion inhibition and sensing in molten chloride systems. Final report. Office of Scientific and Technical Information (OSTI); 2020.10.2172/1734665

[29] Ding W, Shi H, Xiu Y, Bonk A, Weisenburger A, Jianu A, et al. Hot corrosion behavior of commercial alloys in thermal energy storage material of molten MgCl2/KCl/NaCl under inert atmosphere. Solar Energy Materials and Solar Cells. 2018;184:22-30.https://doi.org/10.1016/j.solmat.2018.04.025

[30] Garcia-Diaz BL, Olson L, Martinez-Rodriguez M, Fuentes R, Colon-Mercado H, Gray J. High temperature electrochemical engineering and clean energy systems. Journal of the South Carolina Academy of Science. 2016;14:4. https://scholarcommons.sc.edu/jscas/vol14/iss1/4

[31] Zhang M, Ge J, Yin T, Zhang J. Redox potential measurements of Cr (II)/Cr Ni (II)/Ni and Mg (II)/Mg in molten MgCl2–KCl–NaCl mixture. Journal of The Electrochemical Society. 2020;167:116505.http://dx.doi.org/10.1149/1945-7111/aba15a

[32] Ren S, Chen Y, Ye X-X, Jiang L, Yan S, Liang J, et al. Corrosion behavior of carburized 316 stainless steel in molten chloride salts. Solar Energy. 2021;223:1-10.https://doi.org/10.1016/j.solener.2021.05.057

[33] Mortazavi A, Zhao Y, Esmaily M, Allanore A, Vidal J, Birbilis N. High-temperature corrosion of a nickel-based alloy in a molten chloride environment – The effect of thermal and chemical purifications. Solar Energy Materials and Solar Cells. 2022;236:111542.https://doi.org/10.1016/j.solmat.2021.111542

[34] Lambrecht M, de Miguel MT, Lasanta MI, Pérez FJ. Past research and future strategies for molten chlorides application in concentrated solar power technology. Solar Energy Materials and Solar Cells. 2022;237:111557.https://doi.org/10.1016/j.solmat.2021.111557

[35] Ding W, Gomez-Vidal J, Bonk A, Bauer T. Molten chloride salts for next generation CSP plants: Electrolytical salt purification for reducing corrosive impurity level. Solar Energy Materials and Solar Cells. 2019;199:8-15.https://doi.org/10.1016/j.solmat.2019.04.021

[36] Ding W, Yang F, Bonk A, Bauer T. Molten chloride salts for high-temperature thermal energy storage: Continuous electrolytic salt purification with two Mg-electrodes and alternating voltage for corrosion control. Solar Energy Materials and Solar Cells. 2021;223:110979.https://doi.org/10.1016/j.solmat.2021.110979

[37] Zhao Y, Klammer N, Vidal J. Purification strategy and effect of impurities on corrosivity of dehydrated carnallite for thermal solar applications. RSC Advances. 2019;9:41664-71.https://doi.org/10.1039/C9RA09352D

[38] Zhao Y, Vidal J. Potential scalability of a cost-effective purification method for MgCl2-Containing salts for next-generation concentrating solar power technologies. Solar Energy Materials and Solar Cells 2020;215:110663.https://doi.org/10.1016/j.solmat.2020.110663

[39] Ding W, Shi H, Jianu A, Xiu Y, Bonk A, Weisenburger A, et al. Molten chloride salts for next generation concentrated solar power plants: Mitigation strategies against corrosion of structural materials. Solar Energy Materials and Solar Cells. 2019;193:298-313.https://doi.org/10.1016/j.solmat.2018.12.020

[40] Kurley JM, Halstenberg PW, McAlister A, Raiman S, Dai S, Mayes RT. Enabling chloride salts for thermal energy storage: implications of salt purity. RSC Advances. 2019;9:25602-8.https://doi.org/10.1039/C9RA03133B

[41] Mayes RT, Kurley Iii JM, Halstenberg PW, McAlister A, Sulejmanovic D, Raiman SS, et al. Purification of Chloride Salts for Concentrated Solar Applications. Office of Scientific and Technical Information (OSTI); 2018.10.2172/1506795

[42] Maricle DL, Hume DN. A new method for preparing hydroxide-free alkali chloride melts. United States: Massachusetts Inst. of Tech., Cambridge. Lab. for Nuclear Science; 1959.https://www.osti.gov/biblio/4197980

[43] Pint BA, McMurray JW, Willoughby AW, Kurley JM, Pearson SR, Lance MJ, et al. Re-establishing the paradigm for evaluating halide salt compatibility to study commercial chloride salts at 600°C–800°C. Materials and Corrosion. 2019;70:1439-49. https://doi.org/10.1002/maco.201810638

[44] Li Y, Wang X. Strengthening mechanisms and creep rupture behavior of advanced austenitic heat resistant steel SA-213 S31035 for A-USC power plants. Materials Science and Engineering: A. 2020;775:138991.https://doi.org/10.1016/j.msea.2020.138991

[45] Chai G, Forsberg U. Sanicro 25: an advanced high-strength, heat-resistant austenitic stainless steel. Materials for ultra-supercritical and advanced ultra-supercritical power plants: Elsevier; 2017. p. 391-421.https://doi.org/10.1016/B978-0-08-100552-1.00012-9

[46] Taylor M, Ramirez J, Charit I, Potirniche GP, Stephens R, Glazoff MV. Creep behavior of Alloy 709 at 700° C. Materials Science and Engineering: A. 2019;762:138083.https://doi.org/10.1016/j.msea.2019.138083

[47] Gilardi T, Rodriguez G, Gomez A, Leybros J, Borgard J, Carles P, et al. Influence of material choice on cost estimation of some key components of the sulfur iodine thermochemical process. Proc of 16th World Hydrogen Energy Conference (WHEC)2006. p. 13-6.https://core.ac.uk/download/pdf/37987793.pdf

[48] ASTM-G1-03. Standard Practice for Preparing, Cleaning, and Evaluating Corrosion Test Specimens. 1999

[49] Guo L, Liu Q, Yin H, Pan TJ, Tang Z. Excellent corrosion resistance of 316 stainless steel in purified NaCl-MgCl2 eutectic salt at high temperature. Corrosion Science. 2020;166:108473.https://doi.org/10.1016/j.corsci.2020.108473

[50] Grégoire B, Oskay C, Meißner T, Galetz M. Corrosion mechanisms of ferritic-martensitic P91 steel and Inconel 600 nickel-based alloy in molten chlorides. Part I: NaCl–KCl binary system. Solar Energy Materials and Solar Cells. 2020;215:110659.https://doi.org/10.1016/j.solmat.2020.110659

[51] Skar RA. Chemical and electrochemical characterisation of oxide/hydroxide impurities in the electrolyte for magnesium production: Norwegian University of Science and Technology Fakultet for naturvitenskap og teknologi; 2001.http://hdl.handle.net/11250/244438

[52] Sridharan K, Allen T. Corrosion in molten salts. Molten salts chemistry: Elsevier; 2013. p. 241-67.https://doi.org/10.1016/B978-0-12-398538-5.00012-3

[53] Hanson K, Sankar KM, Weck PF, Startt JK, Dingreville R, Deo CS, et al. Effect of Excess Mg to Control Corrosion in Molten $MgCl_2$ and KCl Eutectic Salt Mixture. Corrosion Science. 2021:109914.https://doi.org/10.1016/j.corsci.2021.109914

[54] Zhu F. Microstructural evolution in austenitic stainless steels for extended-life power station applications: Loughborough University; 2011.https://repository.lboro.ac.uk/articles/thesis/Microstructural_evolution_in_austenitic_stainless_steels_for_extended-life_power_station_applications/9230147

[55] Yamamoto Y, Brady MP, Lu ZP, Maziasz PJ, Liu CT, Pint BA, et al. Creep-resistant, Al2O3-forming austenitic stainless steels. Science. 2007;316:433-6.https://www.science.org/doi/10.1126/science.1137711

[56] Terada M, Escriba DM, Costa I, Materna-Morris E, Padilha AF. Investigation on the intergranular corrosion resistance of the AISI 316L(N) stainless steel after long time creep testing at 600 °C. Materials Characterization. 2008;59:663-8.https://doi.org/10.1016/j.matchar.2007.05.017

[57] Zeng X, Wang X, Li H, Qian C. Strength and creep-fatigue analysis of a molten-salt storage tank. 2019 International Conference on Artificial Intelligence and Advanced Manufacturing (AIAM): IEEE; 2019. p. 742-6.https://doi.org/10.1109/AIAM48774.2019.00153

[58] Mehos M, Price H, Cable R, Kearney D, Kelly B, Kolb G, et al. Concentrating Solar Power Best Practices Study. Office of Scientific and Technical Information (OSTI); 2020.10.2172/1665767

[59] Ding W, Gong Q, Bauer T. Kontinuierliches Reinigungssystem für Halogensalze mit Mg-Additiv. In: DPMA, Filing. Germany2021

[60] Guo J, Hoyt N, Williamson M. Multielectrode array sensors to enable long-duration corrosion monitoring and control of concentrating solar power systems. Journal of Electroanalytical Chemistry. 2021;884:115064.https://doi.org/10.1016/j.jelechem.2021.115064

[61] Choi S, Orabona NE, Dale OR, Okabe P, Inman C, Simpson MF. Effect of Mg dissolution on cyclic voltammetry and open circuit potentiometry of molten $MgCl_2$–KCl–NaCl candidate heat transfer fluid for concentrating solar power. Solar Energy Materials and Solar Cells. 2019;202:110087.https://doi.org/10.1016/j.solmat.2019.110087

[62] Susskind H, Hill F, Green L, Kalish S, Kukacka L, McNulty W, et al. Corrosion studies for a fused salt-liquid metal extraction process for the liquid metal fuel reactor. Brookhaven National Lab., Upton, NY; 1960.https://doi.org/10.2172/4023508